Journal of Power Sources 378 (2018) 125–133

Contents lists available at ScienceDirect

Journal of Power Sources

journal homepage: www.elsevier.com/locate/jpowsour

$CuMn_{1.8}O_4$ protective coatings on metallic interconnects for prevention of Cr-poisoning in solid oxide fuel cells

Zhihao Sun[a], Ruofan Wang[a], Alexey Y. Nikiforov[b], Srikanth Gopalan[a,c], Uday B. Pal[a,c], Soumendra N. Basu[a,b,c,*]

[a] Division of Materials Science and Engineering, Boston University, Brookline, MA 02446, USA
[b] Photonics Center, Boston University, Boston, MA 02215, USA
[c] Department of Mechanical Engineering, Boston University, Boston, MA 02215, USA

HIGHLIGHTS

- $CuMn_{1.8}O_4$ is phase pure spinel at temperatures between 750 °C - 850 °C.
- Conformal and dense coatings on meshes are achieved by electrophoretic deposition.
- There is a reaction layer between Cr_2O_3 and $CuMn_{1.8}O_4$ proved to be $(Cu,Mn,Cr)_{3-x}O_4$.
- 1 mol of $CuMn_{1.8}O_4$ can getter at least 1.83 mol of Cr_2O_3 in at 800 °C.
- Cell tested with coated interconnect exhibits no degradation for 12 days at 800 °C.

ARTICLE INFO

Keywords:
Solid oxide fuel cells
Interconnect
Chromium poisoning
Coating
Copper manganese spinel

ABSTRACT

Cr-poisoning of the cathodes due to the presence of metallic interconnects is detrimental to the performance of intermediate temperature solid oxide fuel cell stacks. Applying a protective coating on the interconnect is an effective solution to preventing Cr-poisoning. In this study, the application of a protective $CuMn_{1.8}O_4$ spinel coating is explored. Dense coatings are deposited on both metallic flat plates and meshes by electrophoretic deposition followed by thermal densification steps. The coating is found to be a mixture of Mn_3O_4 and cubic spinel phases at room temperature but is a pure cubic spinel phase between 750 °C and 850 °C. A reaction layer between the Cr_2O_3 scale at the coating/interconnect interface and $CuMn_{1.8}O_4$ coating is found to be a mixture of $(Cu,Mn,Cr)_{3-x}O_4$ cubic spinel phases with Cr-rich precipitates believed to be Cr_2O_3, indicating that the coating layer acts as a Cr getter. Solubility experiments show that 1 mol of the $CuMn_{1.8}O_4$ phase can getter at least 1.83 mol of Cr_2O_3 at 800 °C. Electrochemical testing of cells in the presence of coated interconnects show that the $CuMn_{1.8}O_4$ coating getters Cr effectively for 12 days at 800 °C, leading to no performance loss of the cell due to Cr-poisoning.

1. Introduction

Solid oxide fuel cells (SOFCs) are devices that convert chemical energy directly into electricity through electrochemical reactions. They have the advantages of high efficiency, fuel flexibility, scalability and environmental friendliness [1,2]. To achieve appropriate voltages, SOFCs need to be stacked in series. In SOFC stacks, adjacent cells are separated by interconnects that have two functions; collecting current from the cells and separating the oxidant on the cathode side and the fuels on the anode side [1]. In intermediate temperature SOFC (IT-SOFC) stacks, Cr_2O_3-forming ferrite stainless steels are found to be the most suitable candidate material due to their coefficient of thermal expansion (CTE) match with other components of SOFCs, high electrical conductivity, low cost and good formability [3]. Cr_2O_3 scales, formed on the surface under the oxidizing atmosphere at operating temperature of SOFCs, provide oxidation resistance to the interconnects. Cr_2O_3 also has significantly higher electrical conductivity compared to other protective oxides such as Al_2O_3 [3,4]. However, formation of Cr_2O_3 also leads to two issues, i.e., i) an increase in the area specific resistance (ASR) since its electrical conductivity though higher than other protective oxides, is still significantly lower than that of stainless steel, and ii) Cr_2O_3 can be further oxidized to Cr^{6+}-

* Corresponding author. 15 Saint Mary's Street, Brookline, MA 02446, USA.
E-mail address: basu@bu.edu (S.N. Basu).

https://doi.org/10.1016/j.jpowsour.2017.12.031
Received 3 October 2017; Received in revised form 2 December 2017; Accepted 12 December 2017

containing gaseous species (such as CrO_3 and $CrO_2(OH)_2$) which can migrate to the cathode and be reduced back as solid-state deposits at the triple phase boundaries. This blocks the electrochemically active reaction sites, causing significant degradation of cell performance [5]. This phenomenon is known as 'Cr-poisoning'.

To alleviate these problems, the growth rate of thermally grown Cr_2O_3 scale should be minimized and the direct contact of this Cr_2O_3 with the oxidant on the cathode side should be avoided. Applying a coating layer on the interconnect surface, that can act as an effective diffusion barrier to inward oxygen diffusion and outward chromium diffusion, is an effective solution. Other requirements for the coating layer include chemical stability, CTE match with the interconnects and high electrical conductivity.

Various materials have been investigated as candidates for interconnect coatings, including reactive element oxides [6,7], perovskites [8,9] and spinels. Of these, spinels exhibit the best ability to inhibit Cr migration [4]. Petric and Ling [10] studied the CTE and electrical conductivities of a large numbers of binary spinels, and concluded that the best candidate materials for coatings are $Mn_xCo_{3-x}O_4$ ($1 < x < 1.5$), $Cu_xMn_{3-x}O_4$ ($1 < x < 1.5$), Co_3O_4 and $CuFe_2O_4$. Of these, $(MnCo)_3O_4$ spinel is considered to be the most promising candidate [11] and has been intensively investigated [12–17]. Cu-Mn spinels, which have higher electrical conductivity [10,13,18] and lower cost, have received much less attention [18–23]. Limited short term studies have shown the potential of Cu-Mn spinel coatings in suppressing the mitigation of Cr while keeping the ASR values within an acceptable range. To further investigate the feasibility of Cu-Mn spinels as a viable coating material, studies of phase stability, interaction with thermally grown Cr_2O_3, properties of their reaction products, and long term performance, are needed.

A variety of deposition methods, such as screen printing [12,17], pulsed laser deposition (PLD) [24], electroplating [19] and electrophoretic deposition (EPD) [21,25,26], have been used for coatings on SOFC interconnects. Of these, screen printing can only be used on flat substrates, while PLD is an expensive line-of-sight process. Electroplating can be used to deposit coatings on complex shapes, but difficulty of deposition of Mn makes it less desirable. In contrast, electrophoretic deposition has low cost due to the simplicity of the apparatus, allows for easy control of coating thickness, and is suitable for mass production on substrates with complex shapes, making it a very attractive method.

To function effectively as a diffusion barrier, the coating needs to be as dense as possible. Since coatings after EPD deposition are not sintered, and are hence very porous, post-deposition densification processing is needed after EPD. In previous studies at Boston University [27], a thermal-mechanical densification method was used on $Cu_{1.3}Mn_{1.7}O_4$ coatings after EPD. The mechanical portion of the densification process involved two uniaxial pressing steps, one after the EPD and the other after annealing the coating in a reducing environment. Uniaxial pressing is not feasible for coatings on complex shapes, and isostatic pressing is required, which would increase process complexity and cost. Therefore, it is highly desirable to develop an effective thermal densification protocol, which eliminates the mechanical pressing steps.

Furthermore, although the $Cu_{1.3}Mn_{1.7}O_4$ coatings mentioned above have high electrical conductivity, the coatings were not stable phase at 850 °C and formed a layer of CuO at the coating surface [27]. To avoid this problem, a Cu-Mn spinel with a lower Cu content, i.e., $CuMn_{1.8}O_4$ was chosen as the coating material. The electrical conductivity of $CuMn_{1.8}O_4$ is ~120 S*cm^{-1} at 800 °C [18], which is slightly lower than that of $Cu_{1.3}Mn_{1.7}O_4$ (~130 S*cm^{-1} at 800 °C [18]), but is much higher than that of the widely used $Mn_{1.5}Co_{1.5}O_4$ (66 S*cm^{-1} at 800 °C [13]).

In this study, $CuMn_{1.8}O_4$ spinel coatings were applied by EPD on Crofer 22 APU plates and Crofer 22 H meshes. A thermal densification method was explored to eliminate the mechanical pressing steps while still achieving dense coatings. The effectiveness of coating layer as a diffusion barrier, its interaction with the thermally grown Cr_2O_3 scale, the time dependence of the area specific resistance (ASR) during high temperature oxidation of the coated samples, as well as the changes in coating morphology, and phase and composition distribution, were studied. Finally, performance of solid oxide fuel cells in direct contact with coated mesh samples were studied to evaluate the ability of the coatings to mitigate the harmful effects of Cr-poisoning.

2. Experimental

2.1. Coating deposition

2.1.1. Preparation of spinel powders

The glycine nitrate process (GNP) was used to prepare the $CuMn_{1.8}O_4$ powders using $Mn(NO_3)_2{\cdot}4H_2O$ (Alfa Aesar, 98%), $Cu(NO_3)_2{\cdot}2.5H_2O$ (Alfa Aesar, 98%) and CH_2NH_2COOH, (Alfa Aesar, 99.5%) as the starting ingredients. The molar ratio of glycine/nitrate ($CH_2NH_2COOH/(Mn(NO_3)_2 + Cu(NO_3)_2)$) used was 0.63, which was previously found to be the optimal ratio for the production of $Cu_{1.3}Mn_{1.7}O_4$ powders [27]. Proportional reactants were dissolved into deionized water, and the solution was heated at 100 °C for 25 min to remove excessive water and formed a gel. The temperature was then slowly raised until combustion occurred. The resulting powders were calcined at 800 °C in air for 2 h to remove possible unreacted components.

Since the EPD process requires a suspension of powders, and the finer particles tend to remain in suspension, the powders were ball-milled with 0.3 mm yttria-stabilized zirconia (YSZ) balls for 4 h in ethanol at a charge ratio (ball to powder mass ratio) of 2:1 using a SPEX SamplePrep 8000 M Mixer/Mill to decrease the particle size. The YSZ balls were then removed by sieving and the spinel powders were suspended in ethanol for the subsequent EPD process.

2.1.2. Electrophoretic deposition process

The interconnect substrates that were coated in this study were 20 mm × 20 mm × 0.1mm Crofer 22 APU plates (Fuelcellmaterials, Lewis Center, OH) and 2 cm^2 discs of Crofer 22 H mesh (Fiaxell SOFC Technologies, Switzerland). The compositions for the two alloys are listed in Table 1. The metallic interconnect substrates were used as the cathode with the anode being a 60 mm × 50 mm Cu plate. The EPD solution consisted of an ethanol and acetone mixture (25:75 vol%, respectively) containing the spinel powders (9 mg ml^{-1}) and I_2 (1.09 mg ml^{-1}). A constant voltage of 20 V was applied for 10 min. The EPD parameters chosen were based on previous reports in the literature [18,21,27]. The coated samples after the EPD process will hereon be referred as the as-deposited samples.

2.1.3. Densification processing

The as-deposited coatings were porous, and had to be subjected to further densification processing. The samples were subjected to a reduction anneal for 24 h at 1000 °C in forming gas (2% H_2 and balance Ar), and then annealed in air at 850 °C for 100 h. The coated samples after the densification processing will be referred hereon as as-processed samples. It should be noted that previous densification processing for a different Cu-Mn spinel ($Cu_{1.3}Mn_{1.7}O_4$) coating included mechanical steps consisting of two separate uniaxial pressings [27], which will not work on mesh samples. In this study, the mechanical steps were eliminated by increasing the temperature and time of the reduction

Table 1
Compositions of Crofer 22 APU [21] and Crofer 22 H [28] (wt%).

Alloy	Cr	Mn	Ti	La	C	P	S	Fe
Crofer 22 APU	22.8	0.45	0.08	0.06	0.005	< .03	< 0.03	balance
Crofer 22 H	22.93	0.43	0.07	0.08	0.007	–	–	balance

anneal.

2.2. Coating microstructure and performance

Phase identification of the spinel powders and the coating layers was carried out by X-ray diffraction (XRD, Bruker D8 Discover system) using CuK_α radiation. ASR measurements were carried out on coated plate substrates by the four-probe method using platinum paste and mesh for electrical contact [21]. The samples were heated at 800 °C for 30 min to cure the platinum paste. Because of the presence of identical coatings on both sides of the substrates, the calculated ASR values were divided by two.

The microstructure and composition of the coatings were studied by field emission scanning electron microscopy (FE-SEM, Zeiss Supra 55VP), scanning/transmission electron microscopy (S/TEM, FEI Tecnai Osiris S/TEM) and energy dispersive X-ray spectroscopy (EDS). Quantifications of the EDS results were carried out by the standardless ZAF method. To prepare SEM specimen, the samples were first mounted in epoxy (EpoThin 2 Resin and Hardener, Buehler), and then polished in cross-section on a Buehler EcoMet 250 Grinder-Polisher using increasing finer silicon carbide abrasive papers (up to 600 grit) before the final polish using 0.05μm alumina polishing suspension. For TEM specimen preparation, samples were mounted and polished identically as the SEM samples, after which electron-transparent cross-sectional TEM samples were made by the *in-situ* lift-out technique using a focused ion beam system (FIB, FEI Quanta 3D FEG), equipped with an Omniprobe micromanipulator.

To test the effectiveness of the coatings in preventing Cr-poisoning in working fuel cells, a coated mesh sample was placed in direct contact with the cathode of a cell and the performance of the cell was measured as a function of exposure time to the interconnect. Detailed information about the setup and cell fabrication can be found elsewhere [29,30]. The cells consisted of a lanthanum strontium manganite (LSM) cathode current collective layer, a LSM/YSZ cathode active layer, a YSZ electrolyte, and a Ni/YSZ anode. A fabricated cell has diameter of approximately 3 cm and active cathode area of approximately 2 cm^2. The tests were carried out at 800 °C with dry air on the cathode side and hydrogen mixed with 2% water vapor as fuel on the anode side. The flow rates of oxidant and fuel were kept at 1000 ml/min and 300 ml/min, respectively. A Princeton Applied Research PARSTAT® 2273 potentiostat and a KEPCO 20-20 M power amplifier were used for the electrochemical testing. The cell was first kept under open circuit voltage (OCV) condition at 800 °C for 2 days for performance equilibration. Then a constant current density of 0.5 A cm^{-2} was applied and the voltage of the cell was measured at every 24 h interval for 10 days. The results were compared to the performances of a cell whose cathode was in direct contact with a commercially available mesh sample with a $CuMn_2O_4$ coating, and a cell whose cathode was in direct contact with an uncoated mesh sample.

3. Results and discussion

3.1. Coating deposition and densification

Fig. 1a (1) shows the XRD result of the powders after calcination at 800 °C in air. It can be seen that the powders are mainly cubic spinel phase with small amount of Mn_3O_4. *In-situ* high-temperature XRD was carried out to confirm the temperature dependence of the phase content of $CuMn_{1.8}O_4$, which will be discussed in section 3.4.

An SEM image of the cross-section of as-deposited coating is shown in Fig. 1b. The coating is uniform and well adherent with a thickness of ~26 μm. Though the particles are densely packed, the as-deposited coating has numerous small pores, thus requiring further densification. Reduction and re-oxidation is an effective strategy for the densification of the coating layer. $Cu_{1.3}Mn_{1.7}O_4$ spinel coatings were found to be reduced to Cu and MnO phases on annealing in forming gas at 850 °C for 1 h [27]. The departure of oxygen during reduction annealing results in increased porosity in the coating layer. The pores in the as-deposited coatings and in the reduced coatings can be reduced by mechanical pressing steps [27]. It was found that without the pressing steps or when the pressure was not high enough, the resulting coatings were highly porous. Although uniaxial pressing is feasible for coatings on flat plates, coatings on complex shapes such as meshes will require the use of isostatic pressing, which is an expensive process. Elimination of the pressing steps is desirable due to a reduction in processing complexity and cost. One way to achieve this is to carry out the densification at sintering temperatures higher than 850 °C. However, sintering in oxidizing atmospheres at high temperatures is not acceptable because it will significantly increase the kinetics of the formation of the Cr_2O_3 scale before the connected porosity is eliminated. An alternative is to increase the temperature and time of the reduction anneal, where densification by sintering can occur in a reducing environment with a low oxygen partial pressure. Lee and co-workers [17] reduced an $Mn_{1.5}Co_{1.5}O_4$ coating at 1000 °C and re-oxidized it at 800 °C without mechanical pressing and achieved a dense coating with a thin layer of oxide scale at the interface. They also reported that a green bar of $Mn_{1.5}Co_{1.5}O_4$ powders subjected to a reduction anneal in forming gas was reduced to Co and MnO. The linear shrinkage of the bar as a result of the sintering of Co and MnO phases increased with increasing temperature, and was as high as 21% linear shrinkage at 1000 °C. This shrinkage was much higher than a green bar of $Mn_{1.5}Co_{1.5}O_4$ powders directly sintered in air at 1000 °C. Since the melting point of Cu (1085 °C) is much lower than that of Co (1495 °C), the sinterability of Cu-MnO phase mixtures should be better than Co-MnO phase mixtures at the same temperature. So it is expected that this strategy would be even more successful for the $CuMn_{1.8}O_4$ coatings.

The as-deposited samples were annealed in a reducing environment (forming gas) at 1000 °C for 24 h. Fig. 1a (2) shows the XRD scan of the coating after reduction. All the peaks in the scan can be indexed to Cu, MnO, and substrate. Fig. 1c shows an SEM image of the sample after reduction. EDS analysis shows the rounded bright particles to be Cu, and the remaining grey areas to be MnO. Compared to the $Cu_{1.3}Mn_{1.7}O_4$ coating after reduction at 850 °C [27], the particle sizes of the Cu in this sample are much larger and the density of the coating layer is much higher. However, there is also a Cr -rich oxide scale with the thickness of ~1.2 μm at the interface. EDS quantification shows that this layer consists of 43.0 at% of O, 36.5 at% of Cr, 19.5 at% of Mn and 1.0 at% of Fe, indicating that this layer is possibly mainly $MnCr_2O_4$. The inaccuracy of O content is because of the limitation of EDS quantification on light elements. This means that oxygen partial pressure at the interface in the forming gas is not low enough to prevent the formation of the thermally grown spinel layer at 1000 °C.

The reduced samples were then re-oxidized at 850 °C in air. As shown in Fig. 1d, the morphology of the coating is completely altered after only 1 h of oxidation annealing. The distinct Cu particles are no longer visible, and at this magnification, the microstructure appears to be homogeneous. However, XRD analysis of the coating after 1 h of oxidation annealing (Fig. 1a (3)) shows that although the majority of the coating at room temperature is the spinel phase, there is also the presence of the Mn_3O_4 phase, as with the spinel powders (Fig. 1a (1)).

3.2. Coating microstructure

Fig. 2a, a higher magnification image of the coating after 1 h of oxidation anneal, shows that the coating is dense with isolated pores and small needle-like structures that are present throughout the coating. Inset in Fig. 2a is an EDS line scan showing the Cr distribution profile in the coating after 1 h of oxidation annealing. The figure shows no Cr diffusion into the coating layer. Fig. 2b shows the coating in cross-section after 100 h of oxidation annealing in air at 850 °C, i.e., the as-processed coating. The figure also shows the Cr distribution profile across the coating, obtained by an EDS line scan. It is evident that with

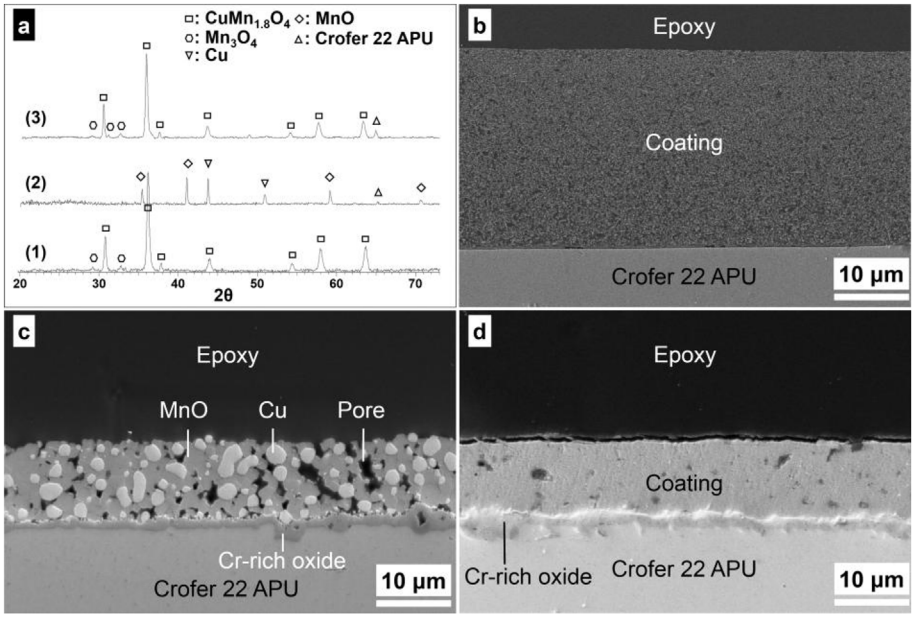

Fig. 1. a) θ - 2θ XRD scans of: (1) $CuMn_{1.8}O_4$ powders after calcination, (2) coating layer after reduction annealing, and (3) coating layer after oxidation annealing for 1 h at 850 °C in air. SEM SE images of $CuMn_{1.8}O_4$ coating in cross-section in the b) as-deposited state after EPD, c) after reduction annealing for 24 h at 1000 °C, and d) after oxidation annealing for 1 h at 850 °C in air.

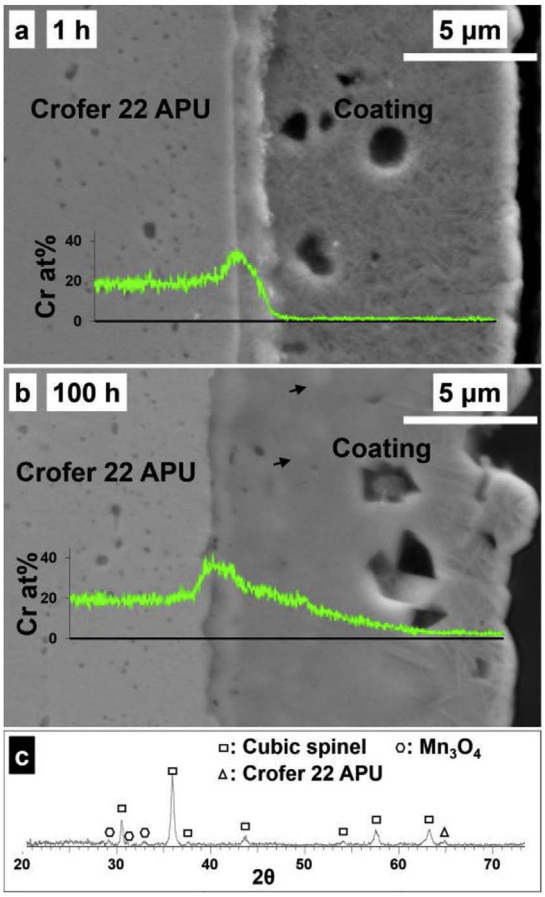

Fig. 2. SEM SE images and Cr distributions along the line shown by x axis of $CuMn_{1.8}O_4$ coating layers after a) 1 h, and b) 100 h oxidation annealing (as-processed sample) at 850 °C in air, c) θ - 2θ XRD scan of as-processed sample.

increasing oxidation time, the coating separates into two distinct layers, an inner Cr-containing dense layer which also has some precipitates (some of which are marked by arrows in Fig. 2b), and an outer Cr-free layer with needle-like structures which are seen in the coating annealed for 1 h. This suggests that the inner dense layer is associated with the presence of Cr. A Cr-rich thermally grown oxide layer can be seen at the coating/substrate interface in Fig. 2b. EDS analysis of this layer showed the composition to be 47.0 at% of O, 52.2 at% of Cr with trace amounts of Mn and Fe, indicating that this interfacial layer is likely Cr_2O_3. Thus the thermally grown $MnCr_2O_4$ formed during the reduction annealing transforms to Cr_2O_3 during the oxidation anneal, implying that once the spinel coating has sintered to sufficient density, the oxygen partial pressure at the substrate/coating interface is low enough to make $MnCr_2O_4$ unstable but high enough for Cr_2O_3 to be stable. An XRD scan of the as-processed coating (Fig. 2c) shows the coexistence of the cubic spinel phase and Mn_3O_4, as with the coating after 1 h oxidation anneal.

The spatial resolution of SEM-based EDS analysis is limited due to the beam size and the beam broadening, which makes the interaction volume to be larger than the sizes of these fine microstructural features such as the precipitates in the dense layer and the needle-like structures in the outer layer. The smaller spot size available in the TEM along with the thin electron transparent sample that limits beam spreading makes TEM-based EDS analysis ideal to study these fine features.

Fig. 3a shows a backscattered electron image of an electron-transparent cross-sectional TEM sample of an as-processed $CuMn_{1.8}O_4$ coating made by the 'lift-out' technique in the FIB. The thinning direction of the Ga beam in the FIB system shown in the figure is from right to left, making the sample thinnest (~300 nm) at the right edge. The pores in the coating are enlarged during FIB processing. Fig. 3b shows a dark-field STEM micrograph of the outer portion of the coating, showing the needle-like structures. Fig. 3c shows a dark-field STEM micrograph of the coating near the interface, which includes the interfacial thermally grown oxide scale and a portion of the Cr-containing inner dense layer. As described in Section 3.3, reaction between Cr_2O_3 and $CuMn_{1.8}O_4$ powders shows the formation of a single-phase Cr-doped copper manganese spinel. We will therefore refer to this Cr-containing dense phase as $(Cu,Mn,Cr)_{3-x}O_4$.

Fig. 4 shows STEM-based EDS elemental dot maps of various regions in the coating. Fig. 4a shows the elemental distribution in the outer layer, indicating that the needle-like structures are rich in Mn and deficient in Cu. A spot spectrum on such a needle-like structure shows a composition of 33.3 at% of Mn, 6.5 at% of Cu, negligible amount of Cr and balance of O. Combined with XRD results (Fig. 2c), it can be concluded that the needle-like structures are Mn_3O_4. Presence of Cu could be caused by beam broadening and/or overlapping between needles-like structures and the surrounding $CuMn_{1.8}O_4$ spinel phase. Fig. 4b shows the EDS elemental maps of the Cr-containing inner dense coating

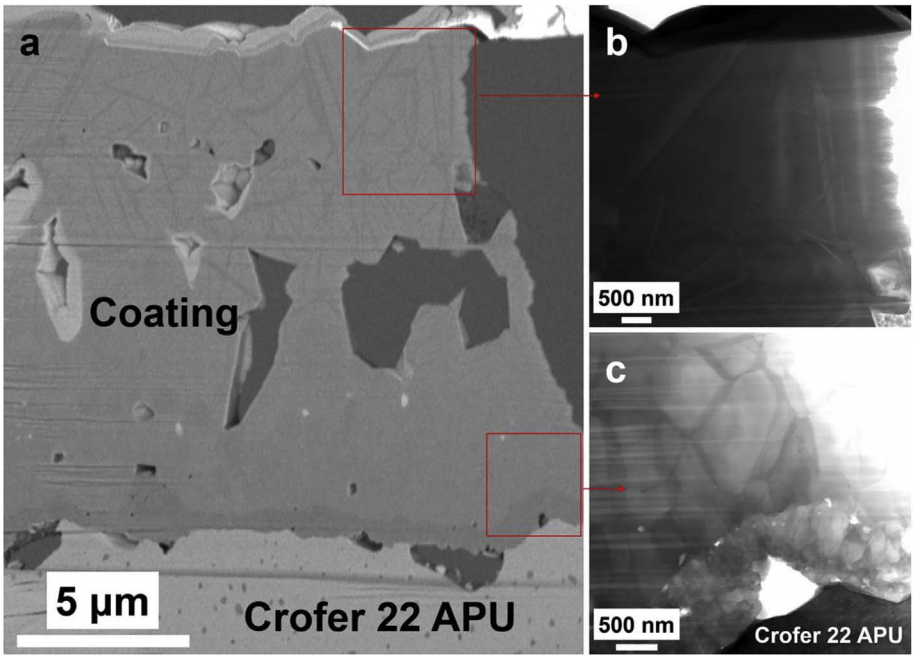

Fig. 3. a) Back-scattered electron image of cross sectional TEM sample, b) STEM dark-field image of needle-like structures, c) STEM dark-field image of inner dense layer and Cr_2O_3 scale.

layer close to the interface. The figures show the presence of Cr-rich precipitates within this layer. It is possible that once the saturation limit of Cr in $(Cu,Mn,Cr)_{3-x}O_4$ is reached, Cr_2O_3 precipitates form. Fig. 4c shows the EDS elemental dot maps from the thermally grown oxide scale at the interface, indicating that the coating is mainly Cr and O, with negligible amounts of Cu, Mn, and Fe. This indicates that the oxide scale is essentially Cr_2O_3, without an outer $MnCr_2O_4$ layer above it, typically found during oxidation of bare Crofer 22 APU [31].

3.3. Interaction between Cr_2O_3 and $CuMn_{1.8}O_4$

Since the previous sections show that Cr can diffuse into $CuMn_{1.8}O_4$ while maintain a cubic spinel structure (Fig. 2c), and that there seems to be a saturation limit after which Cr_2O_3 precipitates out (Fig. 4b), it is important to know the solubility limit of Cr_2O_3 in $CuMn_{1.8}O_4$. To study this experimentally, different molar ratios of $CuMn_{1.8}O_4$ and Cr_2O_3 powders were intimately mixed by ball milling and reacted at 800 °C in air for 10 h. XRD patterns of the resulting powders are shown in Fig. 5.

Fig. 5 shows that for $Cr_2O_3/CuMn_{1.8}O_4$ molar ratios of up to 1.83, a pure cubic spinel phase is the only product, which we have previously designated as $(Cu,Mn,Cr)_{3-x}O_4$. Interestingly, incorporation of increasing amounts of Cr leads to a systematic peak shift to lower 2θ values (e.g., see cubic spinel peaks at 2θ ~ 43.5°), indicating an increase in the lattice parameter. At $Cr_2O_3/CuMn_{1.8}O_4$ molar ratios of 2.01 and higher, the cubic spinel peaks are accompanied by extra peaks that can be indexed as Cr_2O_3, indicating that saturation has been reached. This suggests that $CuMn_{1.8}O_4$ is an excellent getter of Cr (or Cr_2O_3) and at 800 °C, and at least 1.83 mol of Cr_2O_3 (or 3.66 mol of Cr) can be incorporated into each mole of $CuMn_{1.8}O_4$.

3.4. Phase stability of $CuMn_{1.8}O_4$ at different temperatures

In order to study the phase stability of $CuMn_{1.8}O_4$ as a function of temperature, a reduced coating sample (containing Cu and MnO phases) was subjected to two thermal cycles in air and *in-situ* XRD studies were carried out during this process. The heat treatment cycles and the resulting XRD scans are shown in Fig. 6. The sample was first kept at 850 °C for 10 h (scan A) and then cooled to 750 °C and held for 2 h (scan B). The sample was then cooled to room temperature (scan C), and then heated back to 750 °C (scan D) and held for 2 h, before being cooled to room temperature again (scan E). The ramp rates in the thermal cycles were roughly 60 °C min^{-1} and each XRD scan took ~1 h to complete.

It is already known that the re-oxidation of Cu and MnO back to spinel occurs within 1 h of oxidation annealing. So it is expected that $CuMn_{1.8}O_4$ spinel phase is formed at 850 °C after the 10 h oxidation, as confirmed by scan A. Mn_3O_4 peaks, that are present at room temperature (Fig. 1a (3)) do not appear in scan A and scan B. This implies that the $CuMn_{1.8}O_4$ composition is a single-phase spinel at temperatures between 750 °C and 850 °C, which is in the operating range of typical IT-SOFCs. After the sample is cooled down to room temperature, scan C shows that the tetragonal Mn_3O_4 phase appears. Since this phase change happens within 12 min of cooling down, it means that the kinetics of formation of the Mn_3O_4 phase in this material on cooling is rapid. The disappearance of the Mn_3O_4 phase during the heating up to 750 °C, as shown by scan D, indicates that the dissolution of the Mn_3O_4 phase on heating also happens quickly. Scan E is identical to scan C, indicating that the material has no thermal hysteresis in terms of phase changes on heating and cooling. Since Mn_3O_4 only exists at room temperature and disappears very quickly at the operating temperature of SOFCs, its effect on the performance of the coating at operating temperature should not be an issue. The shift of the cubic spinel peaks to lower 2θ values (increased lattice parameters) at high temperature is likely caused by a combination of thermal expansion and Mn_3O_4 incorporation into the lattice. It is also worth noting that there is some broadening of the spinel peaks at room temperature, possibly caused by variation in the composition of the spinel phase resulting from incomplete phase transformation during rapid cooling.

3.5. ASR measurements

ASR measurements were taken during the 100 h processing oxidation annealing at 850 °C to re-oxidize the reduced phases (and obtain as-processed coatings) followed by isothermal oxidation at 800 °C for 400 h in air. The results are shown in Fig. 7a. The ASR gradually increases during both processes, increasing from 8.9 $m\Omega*cm^2$ to 14.9 $m\Omega*cm^2$ during the processing related oxidation annealing, and then increases to 21.8 $m\Omega*cm^2$ after 400 h of isothermal oxidation.

The faster increase of ASR during the oxidation anneal should be caused by faster oxidation kinetics which can be attributed to two

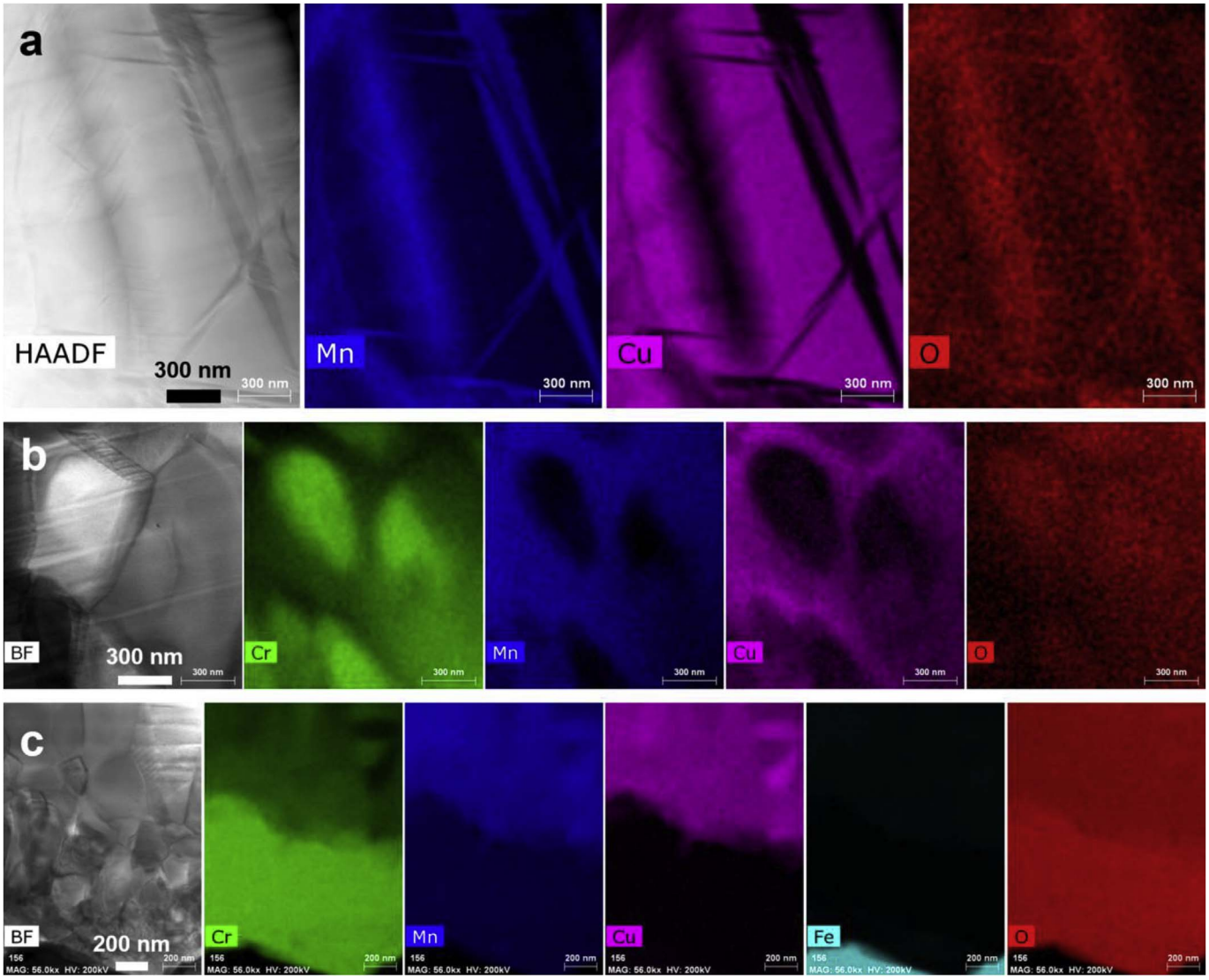

Fig. 4. S/TEM-based EDS elemental dot maps of: a) needle-like structures in the outer coating layer, b) inner dense layer containing precipitates, and c) interfacial oxide scale.

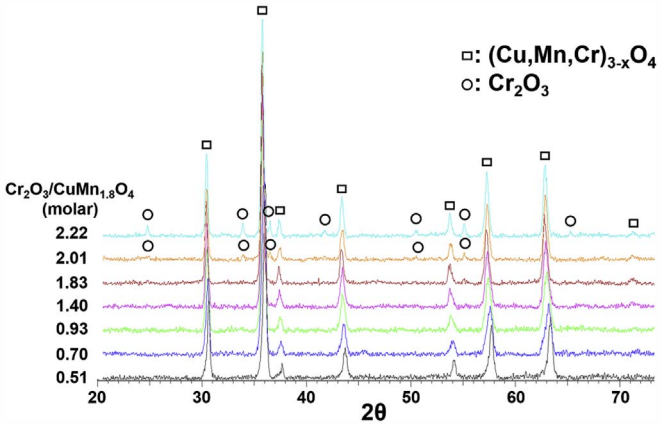

Fig. 5. θ - 2θ XRD scans of products of reactions between $CuMn_{1.8}O_4$ and Cr_2O_3 powders at 800 °C in air for 10 h with different molar ratios of the powders.

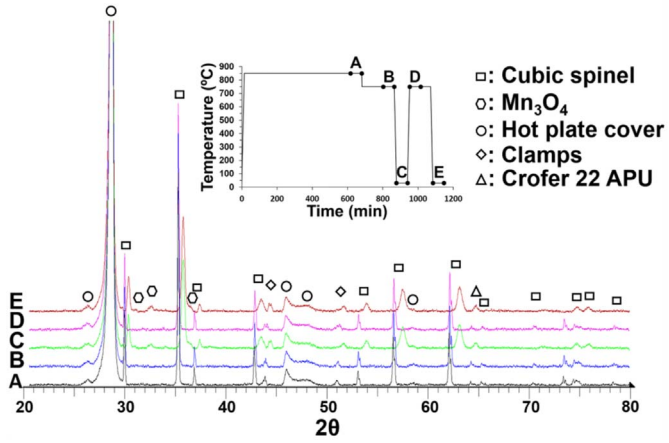

Fig. 6. In-situ XRD scans of reduced coating subjected to two thermal cycles (inset).

factors; the higher temperature (850 °C) and greater probability of connected porosity being present in the as-reduced state than in the as-processed coating after the oxidation anneal. It should be noted that before the measurement, the sample was heated at 800 °C in air for 30 min to cure the platinum paste. Since the re-oxidation of Cu and MnO to spinel is completed in 1 h (Fig. 1d), the ASR measurements shown in Fig. 7a does not reflect the first half hour of the re-oxidation process. It is assumed that the resistances of the platinum paste, mesh, Crofer 22 APU substrate, the silver wires (current leads), and the

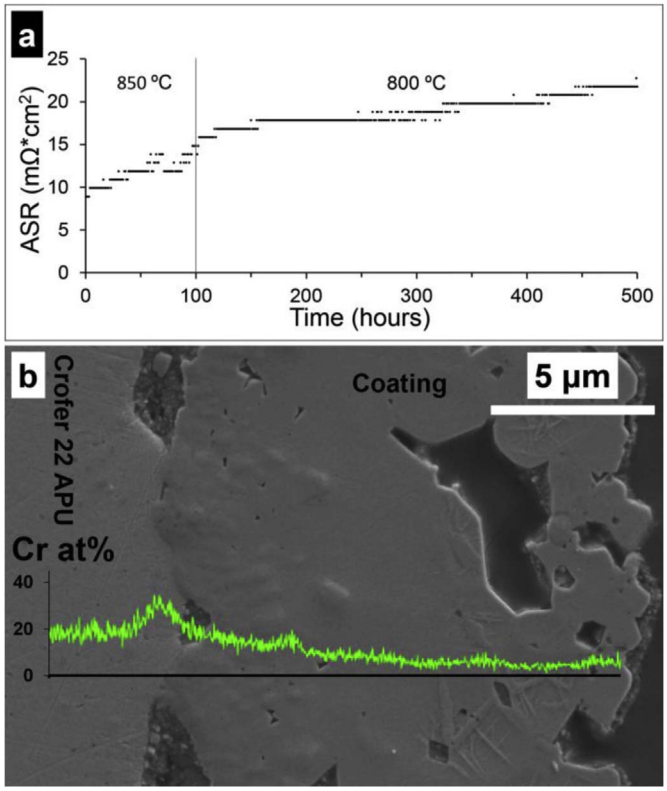

Fig. 7. a) Changes in ASR during the oxidation annealing process (850 °C for 100 h) and during subsequent isothermal oxidation for 400 h at 800 °C in air. b) SEM SE images and Cr distribution along the line shown by x-axis of sample after ASR measurement.

contact resistance are much lower than that of the coating and the Cr_2O_3 scale and thus can be neglected. Since the conductivity of $CuMn_{1.8}O_4$ is ~10^4 higher than that of Cr_2O_3 (~120 S*cm^{-1} [18] to 0.01 S*cm^{-1} [4,5]), which is much larger than the ratio of their thickness (which is ~10, see Fig. 2a), the Cr_2O_3 scale should contribute to ASR much more than $CuMn_{1.8}O_4$ coating. After 100 h of oxidation annealing, the coating has a slightly thinner Cr_2O_3 scale at the interface, as compared to the sample that has undergone oxidation annealing for 1 h (Fig. 2). However, the ASR of the coating goes up between 1 h and 100 h of oxidation annealing. This implies that the formation of the dense $(Cu,Mn,Cr)_{3-x}O_4$ reaction layer plays a role in the ASR increase and that the conductivity of the $(Cu,Mn,Cr)_{3-x}O_4$ reaction layer is lower than that of $CuMn_{1.8}O_4$. The study of electrical properties of $(Cu,Mn,Cr)_{3-x}O_4$ is currently undergoing.

Fig. 7b shows the SEM image and Cr distribution profile of the coating after the ASR testing. Only a small number of needle-like structures exist near the surface of the coating. The EDS line scan shows that Cr has diffused through almost the entire thickness of the coating, indicating that Cr vaporization may happen at this stage. However, most of the coating is still far from the saturation limit, indicating that the coating will still act as a getter for Cr.

3.6. Coating effectiveness in mitigating Cr-Poisoning in cell

The effectiveness of the coatings in mitigating Cr-poisoning were tested in a single cell setup in which the coated mesh interconnects were in direct contact with the cathode of a solid oxide fuel cell. In this setup, mesh samples were chosen to allow air flow to the cathode. Crofer 22 H mesh samples were coated with $CuMn_{1.8}O_4$ using the same EPD process as the flat samples. One advantage of the EPD process is the ease of coating complex shapes with high curvatures. Furthermore, the elimination of the pressing steps in the densification process also facilitates densification of coatings on complex shapes. SEM images of an as-processed mesh sample are shown in Fig. 8. The coating has an excellent coverage of the mesh surface (Fig. 8a). A low magnification cross-section image (Fig. 8b) shows that coating layer is thicker at sharp corners, presumably due to enhanced local electric fields at these locations during the EPD process. A higher magnification micrograph of the coating in cross-section (Fig. 8c) shows the coating to have a similar morphology as coatings on flat plates, indicating that EPD process is transferrable to substrates with complex shapes.

Before the Cr-poisoning test, the cells were first equilibrated at 800 °C for 2 days. Then the cells were run with dry air on the cathode side and humidified (2% water vapor) H_2 on the anode side at a constant current density of 0.5 A cm^{-2}, and the voltage of the cell was measured. Cells in contact with an uncoated sample and with a commercial $CuMn_2O_4$-coated sample were also tested under identical conditions for comparison. Fig. 8d shows the results of the electrochemical tests. It should be noted that the differences in initial cell potentials after cell equilibration are due to different ohmic resistances and different Cr-poisoning effects under open-circuit condition (caused by different partial pressures of Cr vapor species), which has been reported by Wang et al. [32]. The potential of the cell in contact with the uncoated mesh sample started to drop rapidly from the start of the test. For the case of cell in contact with the commercial $CuMn_2O_4$-coated sample, the cell potential increased after the first day, then kept almost constant for next 6 days before dropping. In contrast, the potential of the cell in contact with the $CuMn_{1.8}O_4$-coated mesh sample kept increasing during the entire experimental period. The increase in the cell voltage is associated with cell break-in, a process that occurs initially for all SOFCs being tested for the first time. The decrease in the cell voltage corresponds to the degradation of the cell performance due to Cr-poisoning. The uncoated interconnect has no protective layer to prevent Cr-poisoning, and the cell performance drops immediately. The commercial coating is thin and porous (see inset micrograph in Fig. 8d). Thus the improvement of cell performance on the first day is due to cell break-in, after which the relatively steady performance is due to the balance between cell break-in and Cr-poisoning. After 6 days, the rate of degradation caused by Cr-poisoning is more than the rate of cell break-in, leading to an overall decrease in the cell performance. In the case of the $CuMn_{1.8}O_4$ coating, the cell break-in continues to the end of the testing, indicating that the coating acts as an excellent Cr-getter during this period, thereby mitigating Cr-poisoning.

4. Conclusions

$CuMn_{1.8}O_4$ spinel protective coatings were deposited by EPD on Crofer 22 APU plates and Crofer 22 H meshes in order to prevent Cr poisoning. Dense coatings with isolated pores were achieved by subsequent thermal densification method consisting of a reduction annealing at 1000 °C for 24 h and an oxidation annealing at 850 °C in air for 100 h, thereby successfully eliminating mechanical uniaxial pressing steps that would not be possible on complex shapes such as meshes. $CuMn_{1.8}O_4$ remained a single-phase cubic spinel between 750 °C – 850 °C but formed a separate Mn_3O_4 phase in a needle-like morphology during cooling down to room temperature. The Mn_3O_4 phase however quickly dissolved back into the spinel phase on heating back to high temperature.

During high temperature annealing in an oxidizing atmosphere, a dense reaction layer formed due to the interaction between the spinel coating and the thermally grown Cr_2O_3 scale. This layer was found to be a single phase $(Cu,Mn,Cr)_{3-x}O_4$ cubic spinel phase into which Cr-rich precipitates (most likely Cr_2O_3) were incorporated. It was found that 1 mol of $CuMn_{1.8}O_4$ can effectively getter at least 1.83 mol of Cr_2O_3 at 800 °C. Single cells tested under constant current condition showed that $CuMn_{1.8}O_4$ coatings on Crofer 22 H meshes exhibited excellent Cr-gettering ability for 12 days at 800 °C.

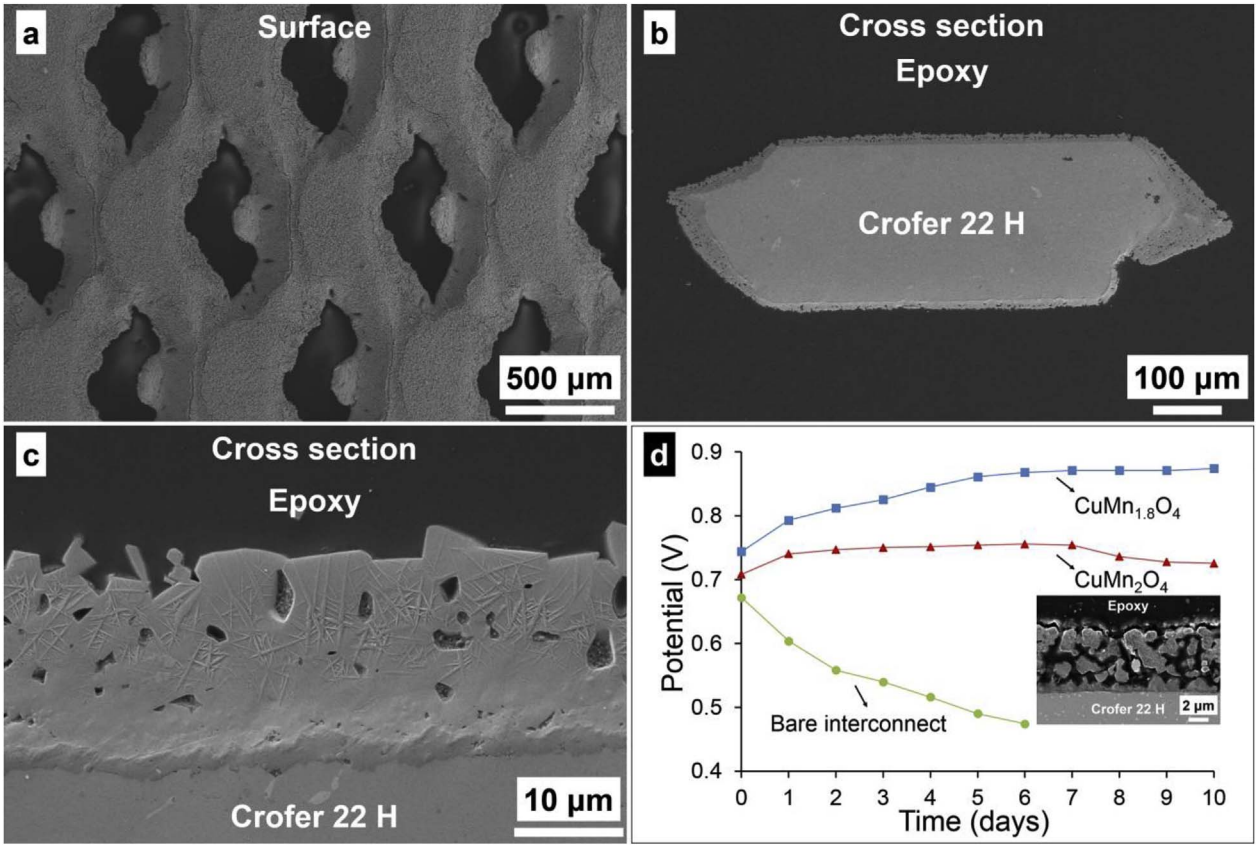

Fig. 8. SEM SE images of the a) surface, and cross-section at b) low-magnification and c) high-magnification of an as-processed Crofer 22 H mesh sample. d) Time dependence of potentials of cells in contact with bare (circles), commercial $CuMn_2O_4$-coated (triangles) and $CuMn_{1.8}O_4$-coated (squares) meshes tested at a constant current density of 0.5 A cm^{-2} at 800 °C. A cross-sectional SEM micrograph of the commercial $CuMn_2O_4$ coating is shown as an inset.

Acknowledgements

This work was supported by the Department of Energy/National Energy Technology Laboratory (award number FE0023325); and National Science Foundation-Major Research Instrumentation (award number 1337471). The authors also acknowledge the use of the FIB/TEM Facility in the Photonics Center at Boston University.

References

[1] EG&G Technical Services, Inc, Fuel Cell Handbook, seventh ed., US DoE, West Virginia, 2004.
[2] R. O'Hayre, S. Cha, W.G. Colella, F.B. Prinz, Fuel Cell Fundamentals, third ed., John Wiley & Sons, New Jersey, 2016.
[3] N. Shaigan, W. Qu, D.G. Ivey, W. Chen, A review of recent progress in coatings, surface modifications and alloy developments for solid oxide fuel cell ferritic stainless steel interconnects, J. Power Sources 195 (2010) 1529–1542.
[4] W.Z. Zhu, S.C. Deevi, Development of interconnect materials for solid oxide fuel cells, Mater. Sci. Eng. A 348 (2003) 227–243.
[5] S.P. Jiang, X. Chen, Chromium deposition and poisoning of cathodes of solid oxide fuel cells–a review, Int. J. Hydrogen Energy 39 (2014) 505–531.
[6] K. Huang, P.Y. Hou, J.B. Goodenough, Reduced area specific resistance for iron-based metallic interconnects by surface oxide coatings, Mater. Res. Bull. 36 (2001) 81–95.
[7] W. Qu, L. Jian, D.G. Ivey, J.M. Hill, Yttrium, cobalt and yttrium/cobalt oxide coatings on ferritic stainless steels for SOFC interconnects, J. Power Sources 157 (2006) 335–350.
[8] J.H. Zhu, Y. Zhang, A. Basu, Z.G. Lu, M. Paranthaman, D.F. Lee, E.A. Payzant, $LaCrO_3$-based coatings on ferritic stainless steel for solid oxide fuel cell interconnect applications, Surf. Coating. Technol. 177 (2004) 65–72.
[9] Z. Yang, G. Xia, G.D. Maupin, J.W. Stevenson, Evaluation of perovskite overlay coatings on ferritic stainless steels for SOFC interconnect applications, J. Electrochem. Soc. 153 (2006) A1852–A1858.
[10] A. Petric, H. Ling, Electrical conductivity and thermal expansion of spinels at elevated temperatures, J. Am. Ceram. Soc. 90 (2007) 1515–1520.
[11] J. Wu, X. Liu, Recent development of SOFC metallic interconnect, J. Mater. Sci. Technol. 26 (2010) 293–305.
[12] Z. Yang, G. Xia, S.P. Simner, J.W. Stevenson, Thermal growth and performance of manganese cobaltite spinel protection layers on ferritic stainless steel SOFC interconnects, J. Electrochem. Soc. 152 (2005) A1896–A1901.
[13] Z. Yang, G. Xia, G.D. Maupin, J.W. Stevenson, Conductive protection layers on oxidation resistant alloys for SOFC interconnect applications, Surf. Coating. Technol. 201 (2006) 4476–4483.
[14] L. Chen, E.Y. Sun, J. Yamanis, N. Magdefrau, Oxidation kinetics of $Mn_{1.5}Co_{1.5}O_4$-coated Haynes 230 and Crofer 22 APU for solid oxide fuel cell interconnects, J. Electrochem. Soc. 157 (2010) B931–B942.
[15] K. Wang, Y. Liu, J.W. Fergus, Interactions between SOFC interconnect coating materials and chromia, J. Am. Ceram. Soc. 94 (2011) 4490–4495.
[16] N.J. Magdefrau, L. Chen, E.Y. Sun, J. Yamanis, M. Aindow, Formation of spinel reaction layers in manganese cobaltite–coated Crofer22 APU for solid oxide fuel cell interconnects, J. Power Sources 227 (2013) 318–326.
[17] S. Lee, J. Hong, H. Kim, J. Son, J. Lee, B. Kim, H. Lee, K.J. Yoon, Highly dense Mn-Co spinel coating for protection of metallic interconnect of solid oxide fuel cells, J. Electrochem. Soc. 161 (2014) F1389–F1394.
[18] M. Galbo, K.J. Yoon, U.B. Pal, S. Gopalan, S.N. Basu, C.K. Belt, Evaluating electrophoretically deposited Cu-Mn-O spinel coatings on stainless steel substrates used in solid oxide fuel cell interconnects, in: A. Jha, C. Wang, N.R. Neelameggham, D.P. Guillen, L. Li, R. Kirchain, J.S. Spangenberger, F. Johnson, A.J. Gomes, A. Pandey, P. Hosemann (Eds.), Proceedings of Energy Technology 2015: Carbon Dioxide Management and Other Technologies, John Wiley & Sons, Inc., Hoboken, NJ, 2015, pp. 333–344.
[19] M.R. Bateni, P. Wei, X. Deng, A. Petric, Spinel coatings for UNS 430 stainless steel interconnects, surf, Coat. Technol. 201 (2007) 4677–4684.
[20] P. Wei, X. Deng, M.R. Bateni, A. Petric, Oxidation and electrical conductivity behavior of spinel coatings for metallic interconnects of solid oxide fuel cells, Corrosion 63 (2007) 529–536.
[21] W. Huang, S. Gopalan, U.B. Pal, S.N. Basu, Evaluation of electrophoretically deposited $CuMn_{1.8}O_4$ spinel coatings on Crofer 22 APU for solid oxide fuel cell interconnects, J. Electrochem. Soc. 155 (2008) B1161–B1167.
[22] N.S. Waluyo, B.K. Park, S.B. Lee, T.H. Lim, S.J. Park, R.H. Song, J.W. Lee, $(Mn,Cu)_3O_4$ based conductive coatings as effective barriers to high-temperature oxidation of metallic interconnects for solid oxide fuel cells, J. Solid State Electrochem. 18 (2014) 445–452.
[23] N. Hosseini, M.H. Abbasi, F. Karimzadeh, G.M. Choi, Development of $Cu_{1.3}Mn_{1.7}O_4$ spinel coating on ferritic stainless steel for solid oxide fuel cell interconnects, J. Power Sources 273 (2015) 1073–1083.
[24] L. Mikkelsen, M. Chen, P.V. Hendriksen, A. Persson, N. Pryds, K. Rodrigo,

Deposition of $La_{0.8}Sr_{0.2}Cr_{0.97}V_{0.03}O_3$ and $MnCr_2O_4$ thin films on ferritic alloy for solid oxide fuel cell application, Surf. Coating. Technol. 202 (2007) 1262–1266.
[25] H. Zhang, Z. Zhan, X. Liu, Electrophoretic deposition of $(Mn,Co)_3O_4$ spinel coating for solid oxide fuel cell interconnects, J. Power Sources 196 (2011) 8041–8047.
[26] Y. Zhang, A. Javed, M. Zhou, S. Liang, P. Xiao, Fabrication of Mn–Co spinel coatings on Crofer 22 APU stainless steel by electrophoretic deposition for interconnect applications in solid oxide fuel cells, Int. J. Appl. Ceram. Technol. 11 (2014) 332–341.
[27] Z. Sun, S. Gopalan, U.B. Pal, S.N. Basu, $Cu_{1.3}Mn_{1.7}O4$ spinel coatings deposited by electrophoretic deposition on Crofer 22 APU substrates for solid oxide fuel cell applications, Surf. Coating. Technol. 323 (2016) 49–57.
[28] B. Kuhn, C.A. Jimenez, L. Niewolak, T. Hüttel, T. Beck, H. Hattendorf, L. Singheiser, W.J. Quadakkers, Effect of Laves phase strengthening on the mechanical properties of high Cr ferritic steels for solid oxide fuel cell interconnect application, Mater. Sci. Eng., A 528 (2011) 5888–5899.
[29] R. Wang, M. Würth, U.B. Pal, S. Gopalan, S.N. Basu, Roles of humidity and cathodic current in chromium poisoning of Sr-doped $LaMnO_3$-based cathodes in solid oxide fuel cells, J. Power Sources 360 (2017) 87–97.
[30] R. Wang, U.B. Pal, S. Gopalan, S.N. Basu, Chromium poisoning effects on performance of $(La,Sr)MnO_3$-based cathode in anode-supported solid oxide fuel cells, J. Electrochem. Soc. 164 (2017) F740–F747.
[31] R. Sachitanand, M. Sattari, J.E. Svensson, J. Froitzheim, Evaluation of the oxidation and Cr evaporation properties of selected FeCr alloys used as SOFC interconnects, Int. J. Hydrogen Energy 38 (2013) 15328–15334.
[32] R. Wang, Z. Sun, U.B. Pal, S. Gopalan, S.N. Basu, Mitigation of chromium poisoning of cathodes in solid oxide fuel cells employing $CuMn_{1.8}O_4$ spinel coating on metallic interconnect, J. Power Sources 376 (2018) 100–110.